Available online at www.sciencedirect.com

SCIENCE DIRECT®

International Journal of Thermal Sciences 45 (2006) 151–167

International Journal of Thermal Sciences

www.elsevier.com/locate/ijts

Role of internal radiation during Czochralski growth of YAG and Nd:YAG crystals

Jyotirmay Banerjee, Krishnamurthy Muralidhar *

Department of Mechanical Engineering, Indian Institute of Technology, Kanpur 208016, India

Received 15 October 2004; received in revised form 27 May 2005; accepted 27 May 2005

Abstract

Crystals of YAG and Nd:YAG are grown from their molten state by the Czochralski technique. Oxide crystals are semi-transparent to infrared radiation. In many instances, radiation losses from the bulk of the crystal and melt are quite large. The scattering of radiation in doped melts can be significant during the growth process. The present study is a numerical simulation of flow and heat transfer during the growth of YAG and Nd:YAG crystals in a Czochralski process. The importance of radiation in the growth process has been examined. The heat flux in the melt comprises of contributions from conduction, advection and radiation. The radiative portion of heat transfer comprises of internal absorption, emission and scattering. It has been calculated in the present work by solving the radiative transfer equation (RTE) simultaneously with the conservation of energy equation. The Czochralski domain is considered to be an isotropically scattering gray medium. The radiative properties are assumed to be independent of wavelength and temperature. The boundaries are taken as diffusely emitting and reflecting opaque surfaces. The results obtained in the present study clearly show that the losses calculated by including internal radiation are higher, when compared to surface radiation alone. In addition, the temperature distribution develops skewness with respect to the crystal axis and thereby influences the shape of the melt–crystal interface. Calculations incorporating the bulk radiation model also show the importance of enclosure conditions for controlling the crystal growth process.

Keywords: Czochralski process; Crystal growth; Absorption; Emission; Scattering; Discrete ordinates; Buoyancy; Marangoni; Rotation

1. Introduction

Oxides crystals such as YAG and Nd:YAG of high quality can be grown from their melt in a Czochralski process. The details of the Czochralski process for individual applications differ in terms of details, but the central idea is as follows. The crucible is initially charged with the polycrystalline material from which the single crystal is to be grown. Thermal energy is supplied by a heater surrounding the crucible, raising the temperature of the charge above its melting point. A seed crystal mounted at the end of a rod, is then dipped into the melt. After an appropriate start-up procedure, the seed is slowly withdrawn from the melt. Under suitable thermal conditions, recrystallization in the form of a single crystal occurs around the original seed. The Czochralski apparatus is schematically shown in Fig. 1(a).

Flow and temperature distribution in the vicinity of the crystal determines the shape of the solid–liquid interface. The curvature of the melt–crystal interface in turn dictates the gross disorders in the grown crystal and hence its quality. The interface shape is thus a quantity of considerable importance.

Fluid flow in the melt arises from a superposition of buoyancy-driven natural convection, thermocapillary-driven Marangoni convection and crystal and/or crucible rotation-driven forced convection. Heat transfer occurs in the form of conduction and convection within the melt, conduction within the crystal, gas convection and radiative exchange between exposed surfaces. In addition, internal radiation can be expected to be important during the growth of oxides, such as YAG. This is because of the high temperatures involved

---

* Corresponding author. Tel.: +91 512 2597182; fax: +91 512 2597408.
E-mail address: kmurli@iitk.ac.in (K. Muralidhar).

1290-0729/$ – see front matter © 2005 Elsevier SAS. All rights reserved.
doi:10.1016/j.ijthermalsci.2005.05.007

Nomenclature

Ar	aspect ratio, $\frac{h_m}{r_c}$	
C_p	specific heat	$\mathrm{J{\cdot}kg^{-1}{\cdot}K^{-1}}$
G	radiant energy impinging on a certain point (irradiation)	$\mathrm{W{\cdot}m^{-2}}$
Gr	Grashof number, $\frac{g\beta(T_w-T_f)r_c^3}{\nu_o^2}$	
h_c	crystal height	m
h_m	melt height	m
Hr	height ratio, $\frac{h_c}{r_c}$	
I	radiation intensity	$\mathrm{W{\cdot}m^{-2}{\cdot}sr^{-1}}$
k	thermal conductivity	$\mathrm{W{\cdot}m^{-1}{\cdot}K^{-1}}$
Ma	Marangoni number $\frac{\frac{d\sigma}{dT}(T_w-T_f)r_c}{\nu_o\mu_o}$	
n	refractive index	
p	dimensionless pressure scaled by $\rho_0\nu_o^2/r_c^2$	
Pr	Prandtl number, $\frac{\nu_o}{\alpha_o}$	
$\mathbf{q}_r$	radiative heat flux vector	$\mathrm{W{\cdot}m^{-2}}$
r	radial coordinate scaled by r_c	
r_c	crucible radius, also characteristic linear dimension	m
Re_{ct}	Reynolds number of crystal rotation, $\frac{\omega r_c^2}{\nu_o}$	
Rr	radius ratio, $\frac{r_s}{r_c}$	
r_s	crystal radius	m
t	dimensionless time	
T	temperature, suffix w for crucible wall and f for fusion point	K
$\mathbf{u}_i$	dimensionless velocities: axial, radial and azimuthal scaled by $\frac{\nu_o}{r_c}$	
w	dimensionless angular momentum whose axis is in the vertical z-direction	
z	dimensionless vertical coordinate along the axis of the crystal and melt	

Greek symbols

α	thermal diffusivity	$\mathrm{m^2{\cdot}s^{-1}}$
β	volume expansion coefficient	$\mathrm{K^{-1}}$
$\tilde{\beta}$	albedo of scattering, $\frac{\varsigma}{\varsigma+\kappa}$	
σ	surface tension	$\mathrm{N{\cdot}m^{-1}}$
$\tilde{\sigma}$	Stefan–Boltzmann constant, $5.67\times10^8\ \mathrm{W{\cdot}m^{-2}{\cdot}K^{-4}}$	
ε	emissivity of the material	
μ	dynamic viscosity	$\mathrm{N{\cdot}s{\cdot}m^{-2}}$
ν	kinematic viscosity	$\mathrm{m^2{\cdot}s^{-1}}$
Ω	solid angle (steradians)	
ρ	density	$\mathrm{kg{\cdot}m^{-3}}$
θ	non-dimensional temperature $(T-T_f)/(T_w-T_f)$	
$\tilde{\xi}, \tilde{\eta}, \tilde{\mu}$	directional coordinates for RTE	
ς	scattering coefficient	$\mathrm{m^{-1}}$
κ	absorption coefficient	$\mathrm{m^{-1}}$
τ	optical thickness $(\kappa\times r_c)$	

Subscripts

i	subscript denoting individual phase
0	subscript denoting the reference phase (melt)
b	subscript denoting the black body

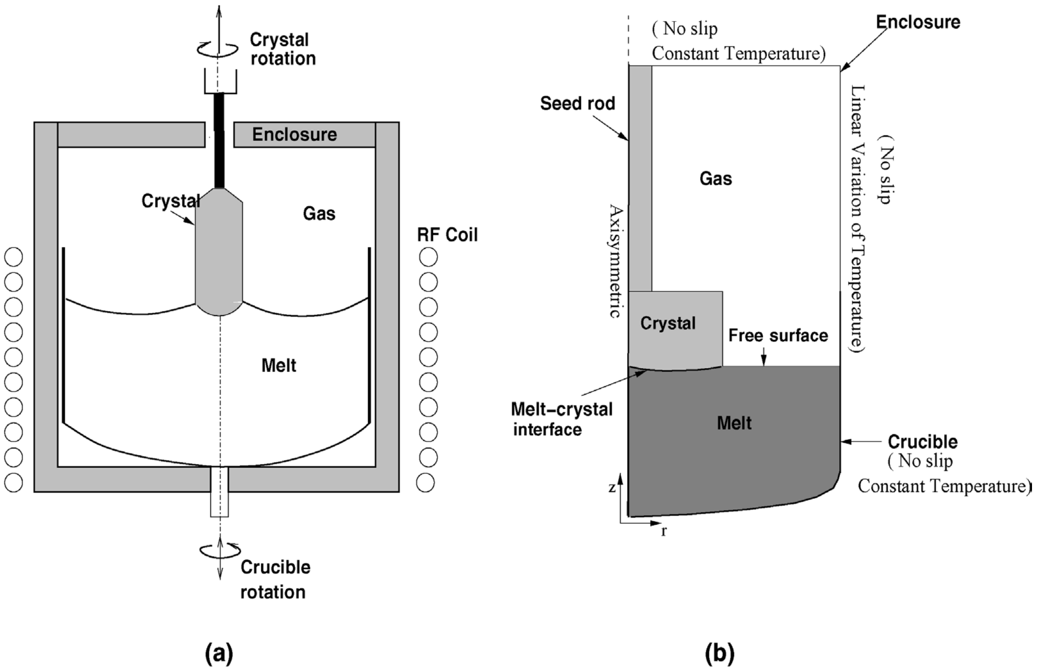

Fig. 1. (a) Schematic diagram of a Czochralski process for growing YAG crystals. (b) Computational domain showing distinct phases in the apparatus.

during their growth and the semi-transparency of these materials to infrared radiation. The YAG melt is doped with Nd atoms that are meant to be incorporated in the grown crystal at a controlled rate. The semi-transparency of the melt and the grown crystal along with scattering enhanced by the dopant particles both in the melt and the grown crystal adds to the overall thermal energy distribution within the Czochralski process.

Several mathematical models of the Czochralski process wherein bulk radiation is incorporated in the governing equations have been reported. Xiao and Derby [1,2] presented analysis of the roles of natural and forced convection in the melt during the growth of oxide crystals. The integrated process model (IPM) developed by Derby and Xiao [3] was employed as the basis of calculations. The model treated radiative transport through the crystal alone, while the melt was considered opaque. Additionally the crystal was assumed to be optically thin, in the sense that only the surfaces within the enclosure have an interaction. Deeply convex interfaces towards the melt, in agreement with experimental results, were predicted by this model. The authors suggested that the interface inversion was dependent on many of the system details including geometry, rather than crystal rotation alone. In these simulations, the Marangoni convection at the gas-melt interface was ignored.

A system analysis of heat transfer in the inductively heated Czochralski furnace was carried out for the growth of oxide crystals by Tsukada et al. [4] with internal radiative heat transfer taken into account. In this model, the crystal and the melt were assumed to be bounded by vanishingly thin semi-transparent diffuse gray surfaces, while the crucible was an opaque, diffuse gray surface. The radiative exchange between the exposed surfaces was calculated using Gebhart's absorption factor method. The effect of optical properties of the melt and crystal on flow and temperature fields for $LiNbO_3$ was investigated. Calculations revealed that the temperature fields are sensitive to the optical properties of the crystal and the melt. The authors observed that the melt–crystal interface shape became more convex towards the melt as the optical absorption coefficients of both the crystal and the melt were lowered. Deflections of the interface increased as the absorption coefficient of the melt increased, for a fixed value of the crystal absorption coefficient.

Kobayashi et al. [5] carried out a numerical study to investigate the importance of internal radiative heat transfer in the melt alone. The model was based on the bulk flow approximation with a focus on the melt convection. The S_N discrete ordinate method was used to solve the equation of radiative transfer. Two types of boundaries considered at the melt surface were: (1) opaque and (2) a semi-transparent diffuse gray melt surface. Flow fields and isotherms were obtained for a wide range of absorption coefficients in the melt. The influence of Marangoni convection was also investigated. The deformation of the melt–crystal interface was however, not discussed.

Nunes et al. [6] combined the multi-zone adaptive grid generation and curvilinear finite volume scheme of Prasad et al. [7] to a spectral thermal radiation model to predict the temperature distribution in a Czochralski domain for growing a YAG crystal. The radiative transfer model was based on the discrete exchange factor method. Absorption and scattering in the crystal phase alone were considered in terms of the albedo of scattering. The individual effects of scattering and absorption were however not brought out in the study.

Kobayashi et al. [8] presented a global simulation of an inductively heated Czochralski furnace. The effect of internal radiative heat transfer in the crystal and melt on the interface inversion was investigated for oxide crystals. The radiative transfer equation in a non-scattering medium was solved using the P_1 method. The general problem of radiative transfer involves determining the radiative intensity from an integro-differential equation in five independent variables—three space coordinates and two additional angles defined at every point. In the P_N method the directional dependence is expressed as a truncated Fourier series representation in spherical harmonics. This step transforms the radiative transfer equation into a system of simultaneous partial differential equations in space coordinates. The index N represents the truncation level, with $N = 1$ being a low order approximation. This level of approximation is suitable for an optically thick medium but not for optically thin regions. The results obtained in the study [8] suggest that for an opaque melt, the critical Reynolds number at which the interface inversion occurs decreases with the optical thickness of the crystal. When the melt is semi-transparent, the critical Reynolds number has a maximum value for a certain optical thickness of the crystal and melt.

The present work reports detailed numerical simulation of flow and heat transfer during the growth of YAG and Nd:YAG crystals in a Czochralski setup (Fig. 1(a)). A eutectic composition of YAG, corresponding to a well-defined melting point temperature has been considered. Absorption, emission, and scattering in the melt as well as the growing crystal are included in the mathematical model. The model is free of the restrictive approximation with respect to optical thickness and has a greater degree of generality. The enclosure condition appears as a significant parameter in the simulation. The importance of radiation in fixing the convection patterns in the melt, shape of the melt–crystal interface and the pull velocity has been parametrically studied.

2. Mathematical formulation

The physical domain consists of the melt in the crucible, the crystal growing out of it, the seed rod, the gas phase and the enclosure. The crucible has a curved base that extends up to 25% of the crucible height. The diameter of the crucible is considered to be equal to that of the enclosure. The transport processes are taken to be axisymmetric, and hence only one half of the apparatus is taken up for analysis. Fig. 1(b) shows the schematic drawing of the right-half of the computational domain considered for analysis along with the applicable boundary conditions.

A stability analysis of buoyancy-driven convection in a Czochralski crucible has not been reported in the literature. Such an analysis would reveal critical values of parameters at which the flow would change patterns become unsteady and ultimately become turbulent. The assumption of axisymmetry in a Czochralski process can be justified since the melt Prandtl number is high. For horizontal differentially heated fluid layer in a Rayleigh–Benard configuration, Krishnamurti [9] has shown that the symmetry patterns are preserved in high Prandtl number fluids ($Pr > 10$) for Rayleigh numbers in excess of 10^4. At very high Rayleigh numbers, the symmetry pattern breaks up and the convective field becomes unsteady. This result is strictly applicable to a horizontal differentially heated fluid layer in a Rayleigh–Benard configuration (the temperature difference being in the vertical direction). For a side heated fluid layer, instabilities appear at a significantly higher Rayleigh number [10] Markatos and Pericleous [11] report 2D turbulent convection in a side heated cavity at a Rayleigh number of 10^{12}. In a Czochralski crucible, the melt experiences temperature differences in the vertical as well as the horizontal directions. In addition, part of the melt surface being exposed to gas phase lowers heat losses and enforces two dimensionality. When radiation is included in the calculation, the overall symmetry of the enclosure is once again felt in the thermal field within the melt. Hence, we may expect axisymmetry in the flow and thermal fields for the range of parameters considered in the present work. Symmetry is further enforced when the crystal is given rotation mainly because it weakens buoyancy-driven flow.

The flow and temperature fields in all the phases can be determined from the conservation equations of mass, momentum and energy. The individual phases in the Czochralski process namely the melt, crystal and gas are treated as regions of constant density. The subscript i indicates the individual phase in which the governing equation is solved. The buoyancy term is treated *via* the Boussinesq approximation. The contribution of radiation is present in the conservation of energy equation. Radiation is one of the modes of transferring thermal energy in a Czochralski process. It must compete with the conductive and convective modes of heat transfer in the melt, solid and gas phases.

The governing equations in dimensionless form are given as follows:

Mass:

$$\frac{\partial \bar{\rho}_i}{\partial t} + \nabla \cdot (\bar{\rho}_i \mathbf{u}_i) = 0 \tag{1}$$

Momentum:

$$\frac{\partial \bar{\rho}_i \mathbf{u}_i}{\partial t} + \nabla \cdot (\bar{\rho}_i \mathbf{u}_i \mathbf{u}_i) = \nabla \cdot (\mu_i \nabla \mathbf{u}_i) - \nabla p - \rho_i Gr\, \theta \hat{\mathbf{k}} \tag{2}$$

Energy:

$$\frac{\partial \bar{\rho}_i \overline{C}_{pi} \theta}{\partial t} + \nabla \cdot (\bar{\rho}_i \overline{C}_{pi} \mathbf{u}_i \theta) = \frac{1}{Pr} \nabla \cdot (\bar{k}_i \nabla \theta) - \nabla \cdot \mathbf{q}_r \tag{3}$$

In the above equations, the thermophysical properties of each phase (represented by suffix i) are non-dimensionalized with that of the melt at its melting point temperature. The unit vector $\hat{\mathbf{k}}$ is along the direction opposed to gravity. The characteristic length, velocity, pressure and temperature used to non-dimensionalize the governing equations and the meaning of the symbols are given in the nomenclature.

When the crystal is rotated, all three components of melt velocity are non-zero. As suggested by Prasad et al. [7] as well as Nunes et al. [6], it is convenient to work with the angular momentum equation rather than the angular velocity. Hence, 2 momentum and 1 angular momentum equation have been solved in the present work.

At the crucible walls and melt/crystal interface, no-slip and the impermeability boundary conditions are applied for all components of velocity. Since velocities are the primary variables in the calculation, pressure boundary conditions cannot be independently prescribed. Instead, pressure is specified as a datum value at the center of the crucible. The boundary pressures are derived from the internal pressure field at the end of the overall computation. Owing to the crystal being pulled, there is an axial component of velocity at the melt/crystal interface. This is ignored in the boundary conditions because the pulling rate (which is around 1 mm·h^{-1} in YAG) is very small compared to other velocity components. The boundary conditions for the angular momentum equation are zero at the crucible walls and free-slip at the melt–gas interface. At the melt–crystal interface it is derived from the no-slip condition in terms of rotational Reynolds number of the crystal as

$$w = Re_{\mathrm{ct}} \times r^2$$

The melt–crystal interface is considered to be isothermal; hence the interface temperature at all times is the fusion point temperature, corresponding to $\theta = 0$. The crucible side walls as well as the curved base are heated, the corresponding boundary condition being $\theta = 1$. Symmetry boundary conditions apply to velocity as well as temperature at the axis of the crucible.

In Eq. (3), the left-hand side represents advection of thermal energy, the first term on the right-hand side is conduction, while the second term on the right-hand side is the radiative contribution. For a semi-transparent medium, radiative heat transfer is evaluated through the divergence of the radiative heat flux, namely $\nabla \cdot \mathbf{q}_r$. It is determined by accounting for absorption, emission and scattering and is given as [5]

$$\nabla \cdot \mathbf{q}_r = \kappa \left(4 \tilde{\sigma} n^2 T^4 - G\right) \quad \text{where } G = \int_{4\pi} I_i \, \mathrm{d}\Omega_i \tag{4}$$

The evaluation of the divergence of the radiative flux $\nabla \cdot \mathbf{q}_r$ at a point within the medium requires a mathematical description of the radiation intensity along all solid angles (Ω_i) at that point within the medium. The intensity distribution can be obtained by solving the conservation equation of radiative intensity, namely the radiative transfer equation (RTE). Along a particular direction ($\hat{\mathbf{s}}$), RTE in an axisymmetric configuration is given as [12–14]:

$$\frac{\tilde{\xi}}{r}\frac{\partial(rI)}{\partial r} + \tilde{\mu}\frac{\partial(I)}{\partial z} - \frac{1}{r}\frac{\partial(\tilde{\eta}I)}{\partial \phi} = \beta S - \beta I \tag{5}$$

where the quantities $\tilde{\xi}$, $\tilde{\eta}$ and $\tilde{\mu}$ are direction cosines and I is the radiation intensity for the discrete direction $\boldsymbol{\Omega}$. The polar angle ϕ is measured from the z-axis. The source term is given as

$$S(\hat{\mathbf{s}}) = (1-\omega)I_b + \frac{\omega}{4\pi}\int\limits_{\Omega_i=4\pi} \Phi(\hat{\mathbf{s}}_i, \hat{\mathbf{s}}) I(\hat{\mathbf{s}}_i)\,\mathrm{d}\Omega_i \tag{6}$$

where $I_b = n^2\tilde{\sigma}T^4$ is the black body radiation.

All the three surfaces (one for the crucible and two for the enclosure) are considered to be diffusely emitting and reflecting, opaque, gray surfaces. The radiative properties such as absorption coefficient and refractive index n are assumed to be independent of temperature and wavelength. The symmetry boundary condition at the axis is written as

$$I_s = I_{s'}$$

For all other surfaces

$$I_s = \varepsilon_s I_b + \frac{(\rho_s)}{\pi}\int\limits_{(\mathbf{n}_s\cdot\boldsymbol{\Omega}_{s'})<0} (\mathbf{n}_s\cdot\boldsymbol{\Omega}_{s'}) I(\Omega_{s'})\,\mathrm{d}\Omega_{s'}$$

where subscripts s and s' denote the outgoing and incoming directions ($\hat{\mathbf{s}}$) to the reflecting surfaces respectively, while ε_s, ρ_s are the emissivity and reflectivity of these surfaces.

The solution of RTE also requires the estimation of the temperature field. Temperature field is obtained by solving the conservation of energy equation (Eq. (3)) that in turn requires the estimation of divergence of radiative heat flux ($\nabla\cdot\mathbf{q}_r$). The strong coupling between RTE and energy conservation equation, has been treated in the present work by the following iterative procedure:

1. Solve the energy equation by neglecting the contribution due to internal radiation, ($\nabla\cdot\mathbf{q}_r$) to obtain an initial guess for temperature distribution.
2. Obtain the black body intensity I_b using this temperature field to solve RTE. Thus obtain the intensity distribution in the physical domain.
3. Use the intensity distribution to obtain the divergence of the radiative heat flux, Eq. (4).
4. Solve the energy conservation equation using the calculated ($\nabla\cdot\mathbf{q}_r$), to update the temperature field.
5. Repeat steps (2)–(4) till convergence in temperature is attained.

3. Solution of conservation equations

The equations of mass, momentum and energy are solved considering a single domain approach wherein the physical parameters are allowed to vary with respect to the individual phases. The individual phases in the Czochralski process (namely the melt, crystal and gas) are treated as regions of constant density, in effect incompressible. The exception is that of the buoyancy term which is treated *via* the Boussinesq approximation. The subscript used for density in the governing equations (1)–(3) indicates the phase in which the governing equations are solved. Thus variation in density permitted in the formulation arises not from changes in pressure and temperature but from a change in the phase itself. The overall computational procedure is based on the numerical treatment of incompressible fluids, in the sense that the pressure is calculated from the mass balance equation and not the equation of state.

Along with the solution of the field equations, it is required to determine the position of the melt–crystal interface and the melt–gas meniscus. The interfaces are tracked as a 1-dimensional entity in a 2-dimensional Euclidean space. The position and velocity of the melt–crystal interface are governed by energy balance between the heat flux on each side of the interface and the latent heat release. The position of melt–gas meniscus on the other hand is governed by a force balance among the viscous, pressure and the surface tension forces. A gradient in surface tension introduces Marangoni number as an appropriate dimensionless quantity in the simulation. Computations showed that the gas–melt interface was practically flat for the range of parameters studied. In addition, the mechanical coupling between the melt and the gas phase was negligible, while thermally coupling was significant. This is to be expected for fluid–fluid interfaces that have a great viscosity contrast.

The governing field equations for the entire domain is solved using a control volume formulation based on the SIMPLER algorithm. The irregular shape of the interfaces and curved crucible base are allowed to evolve in response to the process parameters. Numerically they have been treated using coordinate transformation and body fitted grids. The transformation from the physical space to the computational space is attained in such a way that the melt–crystal interface as well as the free surface are made to align with orthogonal coordinate lines. Grids are generated so as to maintain orthogonality along these surfaces. This facilitates easy implementation of the boundary conditions at these surfaces, particularly the Marangoni boundary condition at the gas–melt free surface. The numerical treatment of the conservation equations follows closely the work of Prasad et al. [7].

3.1. Solution of RTE

The solution of RTE determines the radiative flux, that is a source term for the energy equation. The numerical treatment of this equation is discussed below.

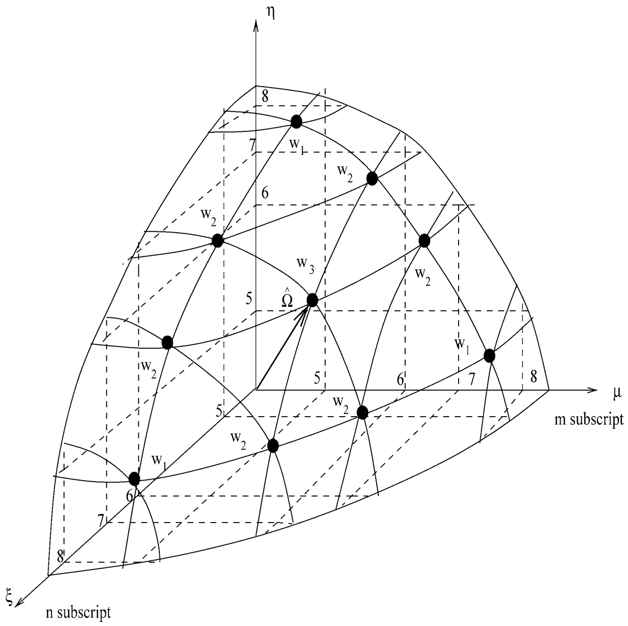

Fig. 2. Points representing directions on the surface of a sphere with unit radius. The points shown are for the octant where $\tilde{\mu} \geqslant 0$, $\tilde{\xi} \geqslant 0$, $\tilde{\eta} \geqslant 0$. The number of points shown is for an S_8 solution.

The S_N discrete ordinates method originally proposed by Chandrasekhar [15] and described by Modest [12] has been used in the present work to discretize the RTE (Eq. (5)). In essence the S_N discrete ordinates method is a numerical technique that solves the RTE along a number of discrete directions spanning the range of a solid angle of 4π. A sketch of the directions used for a S_8 solution is shown in Fig. 2 as points on the surface of a unit sphere. A directional vector from the origin piercing the surface of the sphere at each of these points gives the directions in which the RTE is solved. The total number of discrete directions, P, for a given S_N solution is

$$P = \frac{2^d N(N+2)}{8} \tag{7}$$

where d represents the dimensionality of the problem and N is the number of directions used in S_N. The above equation is useful only for even values of N. In the present work, values of $d = 2$ and $N = 4$ have been used, yielding $P = 12$.

Once all the directions are defined, it remains to specify the directional weights, $w_{m,n}$. The weights are a measure of the solid angle associated with each direction. Combined with the directional cosines they lead to a numerical scheme for performing discrete angular calculations and angular integration. The weights and direction sets used in the present work have been adopted from [12,16].

It is difficult to discretize the third term of Eq. (5); hence an energy balance on a finite spatial and directional control volume is performed to obtain the numerical version of this equation. Following [17–19], the discretized form of the RTE is written as

$$\begin{aligned}
&\tilde{\mu}_m(A_{i,j+1/2}I_{i,j+1/2,m,n} - A_{i,j-1/2}I_{i,j-1/2,m,n}) \\
&\quad + \tilde{\xi}_n(A_{i+1/2,j}I_{i+1/2,j,m,n} - A_{i-1/2,j}I_{i-1/2,j,m,n}) \\
&\quad + (A_{i,j+1/2} - A_{i,j-1/2}) \\
&\quad \times \left[\frac{\alpha_{m+1/2,n}I_{i,j,m+1/2,n} - \alpha_{m-1/2,n}I_{i,j,m-1/2,n}}{w_{m,n}}\right] \\
&= \beta V_{i,j}(S_{i,j} - I_{i,j,m,n})
\end{aligned} \tag{8}$$

The subscripts on the intensities, namely i and j represent the axial and radial location of the central point of the spatial control volume. When i or j is reduced or enhanced by $1/2$, the respective spatial control volume face is indicated. The subscripts m and n represent the center of the directional control volume. The subscript m represents the $\tilde{\mu}$ level under consideration, and n the $\tilde{\xi}$ level. Enhancing or diminishing these subscripts by $1/2$ indicates a point on the face of the directional control volume. The subscripts on the area A indicate the face of the spatial control volume, while the subscripts on the volume V indicate the spatial control volume. The third term in the above equation is different from the first two terms. The first two terms have known spatial areas and directional cosines as coefficients of intensities, while the third term has the unknown quantity α as a coefficient for the areas. The coefficients in the directional control volume term are determined by solving the discretized RTE in an isothermal enclosure [12,16]. In an isothermal enclosure, blackbody radiation at the temperature of the enclosure prevails at all locations and in all directions. This greatly simplifies the above equation and yields

$$\alpha_{m+1/2,n} = \alpha_{m-1/2,n} - w_{m,n}\tilde{\mu}_m$$

The values $\alpha_{N/2-n+1/2,n} = 0$ for $1 \leqslant n \leqslant N/2$ and $\alpha_{n-N/2-1/2,n} = 0$ for $N/2 \geqslant n \geqslant N$ are used to start the recursion relation for every $\tilde{\xi}$ level.

An examination of the discretized form of RTE (Eq. (8)) shows that there are eight intensities that need to be determined, the source function comprising of one blackbody intensity. Three of the seven intensities are determined in terms of those calculated at the adjacent spatial and directional control volumes (namely, boundary conditions). This leaves four intensities that need to be determined. One of these four intensities is determined from the discretized form of RTE; others are obtained by making suitable assumptions on how the intensities at the control faces are related to the intensity at the control volume. Assuming γ_r, γ_z, γ_ϕ as the interpolation factors in r, z and ϕ directions respectively, we get

$$I_{i,j,m,n} = \gamma_r I_{i,j+1/2,m,n} + (1-\gamma_r)I_{i,j-1/2,m,n}$$
$$I_{i,j,m,n} = \gamma_z I_{i+1/2,j,m,n} + (1-\gamma_z)I_{i-1/2,j,m,n}$$
$$I_{i,j,m,n} = \gamma_\phi I_{i,j,m+1/2,n} + (1-\gamma_\phi)I_{i,j,m-1/2,n}$$

The three equations are used to eliminate the downstream intensities from the discretized version of RTE. The resulting expression can then be solved for the center-point intensity in terms of the upstream intensities. Once the centre point intensity is found, the above difference equations yield the downstream control face intensities as well. The weighing functions are suitably selected to avoid unrealistic negative values of intensities.

From the equations presented above the radiative intensity as a function of position, direction and temperature can be obtained. With radiative intensity known, the radiant energy impinging on a certain point can be obtained from the discretized form of Eq. (4) as

$$G_{i,j} = \sum_{n=1}^{N/2} \sum_{m=N/2-n+1}^{N/2+n} I_{i,j,m,n} w_{m,n} + \sum_{n=N/2+1}^{N} \sum_{m=m-N/2}^{3N/2-n+1} I_{i,j,m,n} w_{m,n} \tag{9}$$

This value is now used to calculate radiative source term $\nabla \cdot \mathbf{q}_r$ (Eq. (4)) and subsequently used in the equation of conservation of energy for the calculation of temperature.

3.2. Code validation and grid independence

Validation studies including buoyancy and rotation, flow and heat transfer, steady and unsteady convection were conducted in the following manner. The computer code was initially validated against the experiments of [21] and the unsteady numerical simulation of [22,23]. The comparison, discussed by Banerjee [24] was found to be excellent.

The radiation calculations have been validated against the analytical results of Dua and Cheng [20]. The analytical solution is applicable for a gray, cylindrical column of isothermal gas held in an enclosure at the same temperature. The configuration considered in the validation exercise is shown in Fig. 3 wherein a cylindrical column of semi-transparent material and its midplane are shown. The length-to-radius ratio of the cylinder is two. Under radiative equilibrium conditions, the governing equations are linear in T^4, and hence temperature need not be explicitly specified. Dua and Cheng [20] have presented profiles of average dimensionless radiation intensity as a function of radial position at the midplane for three different optical depths. These results are compared against the simulation based on DOM in Fig. 4. A good match between the two approaches is to be seen, the maximum difference anywhere in the gas being less than 1%. Minor differences arise from the use of a finite number of discrete ordinates ($= 4$) for comparison. The agreement validates the discrete ordinates method and its implementation in the present study. The degree of agreement with an analytical solution also points towards the accuracy of DOM.

To validate the numerical algorithm including buoyancy-driven fluid motion and radiation, the configuration of Kobayashi et al. [5] has been considered. The isotherm patterns in a Czochralski crucible obtained in the present simulation as against the work of [5] are compared in Fig. 5. The material in the crucible is $LiNbO_3$. The sensitivity of the convective field to absorption coefficient is brought out in the figure. The comparison between the present work and the reference is not quantitatively exact. Differences are to be traced to the fact that some of the boundary conditions of Kobayashi et al. [5] involving the crucible material could not be truly reproduced in the present study. The comparison is however, qualitatively satisfactory; the sensitivity of the flow field to the absorption coefficient is also correctly brought out.

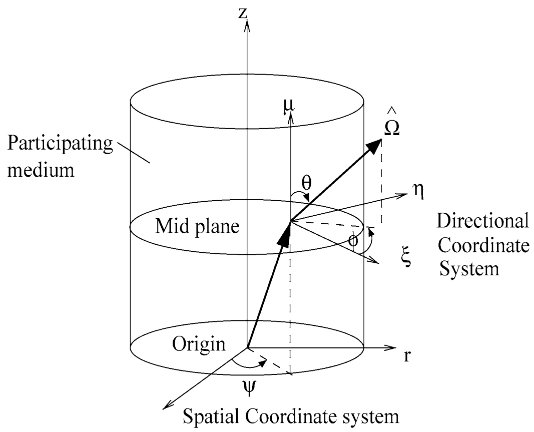

Fig. 3. Spatial and directional coordinate systems used for radiation calculations [19].

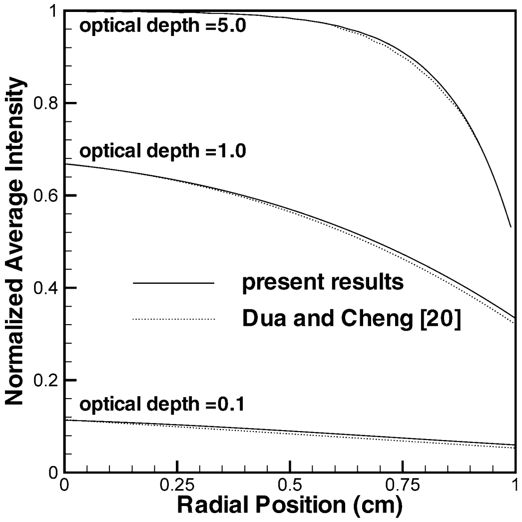

Fig. 4. Comparison of results obtained by DOM with the analytical results of Dua and Cheng [20], in terms of normalized average intensity profiles at the midplane of a cylindrical, emitting, absorbing column of isothermal gas with non-emitting, non-reflecting boundaries.

The grid independence study has been conducted using the maximum velocity and the heat flux through the melt–crystal interface as the sensitivity parameters. Grid independent solutions were obtained for a grid size of 160 × 80 in the complete Czochralski domain, with a grid of 80 × 80 for the melt domain and 40 × 40 for the crystal domain. These grids pertain to an aspect ratio $Ar = 1$, height ratio $Hr = 0.5$ and radius ratio $Rr = 0.5$. In other simulations, the grid points in the melt and crystal region are proportionately allocated

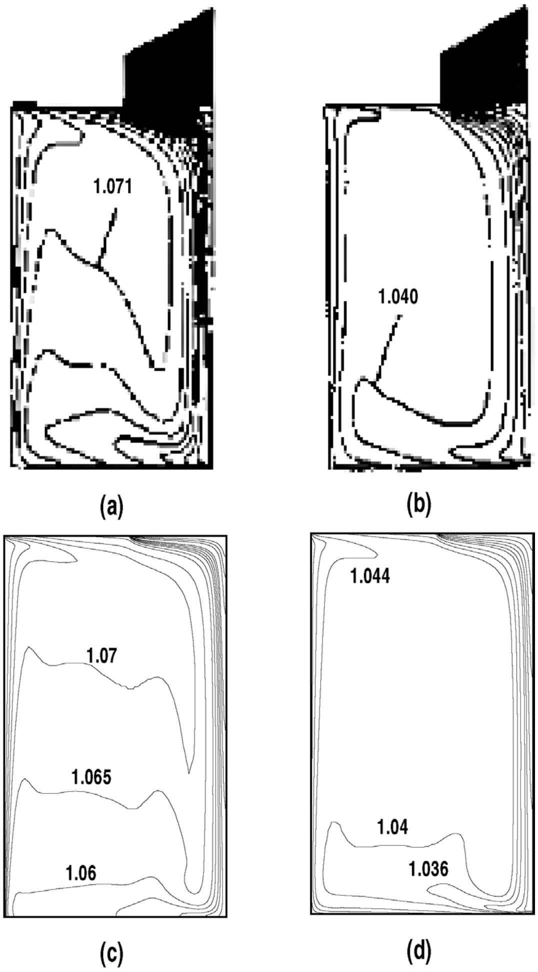

Fig. 5. (a, b) Isotherms obtained by Kobayashi et al. [5] for flow in $LiNbO_3$ melt. Physical parameters considered were $Pr = 13.6$, $Gr = 4.67 \times 10^5$, $Ma = 0$, (a) $\kappa = \infty$ and (b) $\kappa = 0.01$; (c, d) Isotherms obtained in the present work for flow in $LiNbO_3$ melt. Physical parameters considered are $Pr = 13.6$, $Gr = 4.67 \times 10^5$, $Ma = 0$, (c) $\kappa = 30$ and (d) $\kappa = 0.01$.

with respect to the radius ratio of the crystal and the aspect ratio of the melt.

Simulations considered for this study are for temperature differences of 160 and 200 K between the crucible wall and the melting point of YAG (= 2243 K). The thermophysical properties utilized in the study are summarized in Table 1. A typical crucible diameter considered is 100 mm. These data corresponds to Grashof numbers 2.16×10^4 and 2.7×10^4 and Marangoni numbers 475 and 593, respectively. The crystal rotation rates considered are 0 and 20 rpm which correspond to Reynolds numbers of 0 and 408, respectively.

4. Results and discussion

Internal radiation calculations are highly sensitive to properties such as refractive index, absorption coefficient and the scattering coefficient. Widely varying values of absorption coefficients for YAG have been reported in Refs. [25,26]. To examine the sensitivity of the solution to these quantities, a parametric study has been taken up by varying the absorption and scattering coefficients over a certain range. The nominal values of the radiation properties of YAG are listed in Table 2. The following sections present results of numerical simulation obtained for the YAG melt ($Pr = 9.2$) in the crucible alone, and when it is a part of the entire Czochralski apparatus. The interaction of radiation and convection in terms of flow patterns, isotherms, the shape of the melt–crystal interface, and the pull velocity are discussed.

Table 1
Thermophysical properties of molten YAG used in the simulation. Subscripts l and g denote melt and gas, respectively

Description	Symbol	YAG
Density (liquid)	ρ_l	$3600\ \mathrm{kg{\cdot}m^{-3}}$
Thermal conductivity (liquid)	k_l	$4.0\ \mathrm{W{\cdot}m^{-1}{\cdot}K^{-1}}$
Melting point	T_f	2243 K
Melt expansivity	β	$1.8 \times 10^{-5}\ \mathrm{K^{-1}}$
Viscosity (liquid)	μ_l	$4.68 \times 10^{-2}\ \mathrm{kg{\cdot}m^{-1}{\cdot}s^{-1}}$
Heat capacity (liquid)	c_l	$800\ \mathrm{J{\cdot}kg^{-1}{\cdot}K^{-1}}$
Heat of fusion	H_f	$4.55 \times 10^5\ \mathrm{J{\cdot}kg^{-1}}$
Emissivity (liquid)	ε_l	0.3
Surface tension (liquid)	σ_c	$0.65\ \mathrm{N{\cdot}m^{-1}}$
Surface tension coefficient (liquid)	$\frac{d\sigma}{dT}$	$-3.5 \times 10^{-5}\ \mathrm{N{\cdot}m^{-1}{\cdot}K^{-1}}$
Prandtl number	Pr	9.2

Table 2
Spectrally and hemispherically averaged radiative properties of YAG at an average temperature of 2000 K

Radiative parameters	Mean value	Variation
Absorption coefficient	$5.0\ \mathrm{m^{-1}}$	$0–100.0\ \mathrm{m^{-1}}$
Scattering coefficient	$500.0\ \mathrm{m^{-1}}$	$0–1000\ \mathrm{m^{-1}}$
Reactive index of YAG	1.82	
Emissivity of enclosure surface	0.3	
Emissivity of crucible wall	0.3	
Emissivity of melt surface	0.3	

4.1. Melt convection

Solidification of the material in crystalline form in a Czochralski crucible is initiated by cooling the melt through one or more boundaries. Thus temperature gradients are established within the superheated molten material. Since fluid density is sensitive to temperature, the corresponding density gradients result in buoyancy-driven convection, a major driving force for fluid motion in the crucible. In order to improve structural and stoichiometric uniformity and to smooth out thermal asymmetries in a growing crystal, the growing crystal is rotated about its axis, as it is pulled. The rotating crystal acts as a centrifugal pump drawing the liquid melt axially, while ejecting it in the radial direction. In addition to natural and forced convection, the Czochralski process has thermocapillary (Marangoni) flow near the melt–gas free surface. Since the coefficients of surface tension of most crystal materials in their molten form vary with temperature, a non-zero temperature gradient along the free surface causes a non-constant surface traction, resulting in a finite shear at the free surface. The flow pattern is further complicated by the heat losses (convective and radiative) at this boundary.

Buoyant convection in a YAG melt produces melt–crystal interfaces that are convex into the melt. When the crystal is given a rotation, the centrifugal forces drive a clockwise roll that counteracts the thermally driven flow. Thus, when a critical rotation rate is exceeded, the interface shape changes from convex to flat, and subsequently becomes concave. The critical rotation rate has been identified as a function of the radius ratio and aspect ratio. When thermocapillarity at the free surface of the melt is included in the model, circulation due to buoyancy-driven convection is strengthened. The superposition of these two flow mechanisms leads to deeply convex melt–crystal interface.

4.2. Influence of internal radiation on melt convection

Flow and heat transfer in the semi-transparent YAG melt contained in the Czochralski crucible is taken up in this section. The melt absorbs, emits and scatters radiation. The free surface exposed to gas is taken to be flat; further, it is assumed to be an opaque and diffuse gray surface. The melt–crystal interface is at the melting point temperature and is also assumed to be an opaque gray surface. Other parameters employed in the simulation are listed in Table 2. For the discussion in the present section, the changes in the thermal field within the crystal do not influence the calculation. In this respect, the crystal is passive. However, the crystal serves to enforce an isothermal boundary condition at the melt–crystal interface. In addition, it can impart rotation to the melt as well. The effect of thermal gradients in the crystal and energy exchange with the enclosure are considered in Section 4.3.

Energy transferred by radiation at the melt–gas free surface to the radiatively black wall of the enclosure at a temperature T_∞, is determined as follows. The energy balance equation at the free surface (denoted by subscript s) is written as

$$-k_l \frac{\partial T}{\partial n}\bigg|_s = \tilde{\sigma}\varepsilon_l\big(T_s^4 - T_\infty^4\big) + \varepsilon_s I_{b,s} + (1-\varepsilon_s)\int\limits_{(\mathbf{n}_s\cdot\boldsymbol{\Omega})<0} (\mathbf{n}_s\cdot\boldsymbol{\Omega})\, I(\Omega)\,\mathrm{d}\Omega \qquad (10)$$

Here, suffix l stands for the melt properties. For the present work, the free surface properties have been taken to be identical to those of the melt. Exceptions are possible when the free surface is contaminated.

Eq. (10) incorporates the assumption that the free surface is opaque. The first term on the right-hand side represents losses from the free surface to the enclosure. The remaining terms define energy exchange between the free surface and the crucible, and include geometrical factors. Since the free surface is opaque, radiation from the crucible does not reach the enclosure, and is redistributed in the melt. Eq. (10) forms the free surface boundary condition for temperature in the energy equation.

4.2.1. Effect of absorption

Fig. 6 shows the flow and thermal fields in the semi-transparent melt of YAG as the absorption coefficient (κ) and hence the optical thickness (τ) are increased. The zero absorption result, corresponding to a non-participating medium, is included for comparison. The right half of the cavity comprises of streamlines, while the left half carries isotherms. The arrow affixed to streamlines indicates the direction of fluid motion. The direction of fluid motion is important because flow direction changes from clockwise to counter-clockwise, depending on the choice of process parameters. The isotherms shown in Fig. 6 are equally spaced with an increment of $\Delta\theta = 0.1$. It is clear that absorption of radiation does not influence the strength of convection, the maximum in the stream function being practically unchanged. The temperature levels are however, affected. In addition, the changes in the thermal field lead to a significant re-distribution of the flow.

The distribution of isotherms shows a preferential bunching near the crucible walls. This effect increases with the absorption coefficient. Bunching of isotherms near the crucible wall was earlier observed by Kobayashi et al. [5] for simulation of $\mathrm{LiNbO_3}$ ($Pr = 13.6$) melt. A possible explanation for this effect is that the radiant energy from the high temperature wall of the crucible is absorbed in the melt near the wall itself. As a result of bunching, melt at a lower temperature below the crystal shifts towards the wall. The isotherms are increasingly packed near the crucible wall for higher values of the absorption coefficient. The flow structure is organized when there is no absorption, but gets distorted when the absorption coefficient increases. The flow intensity is slightly larger at an intermediate value of optical thickness ($\tau = 0.075$). This is depicted by the largest value of stream function in the individual figures. The intensity of convection marginally decreases at higher values of absorption coefficient. The centre of the convection cell setup by the combined effect of buoyancy and Marangoni forces shifts upwards, closer to the melt free surface as the absorption coefficient increases. Further, there is a horizontal shift in the cell-centre towards the crucible side wall.

A remarkable change in the flow structure of the melt occurs at a very high value of the optical thickness (Fig. 6(d)). The flow pattern consists of two cells. The appearance of two cells is explained by the fact that a great deal of radiant energy does not reach the central region of the melt. The crucible is incapable of sufficiently heating the bulk of the melt. This leads to low temperatures at the central region when compared to the crucible walls and the axis. Cooling of the core has been reported by Xiao and Derby [1] for simulation of GGG melt ($Pr = 6$). The lower temperature in the core drives two convective loops in the crucible. The inner loop

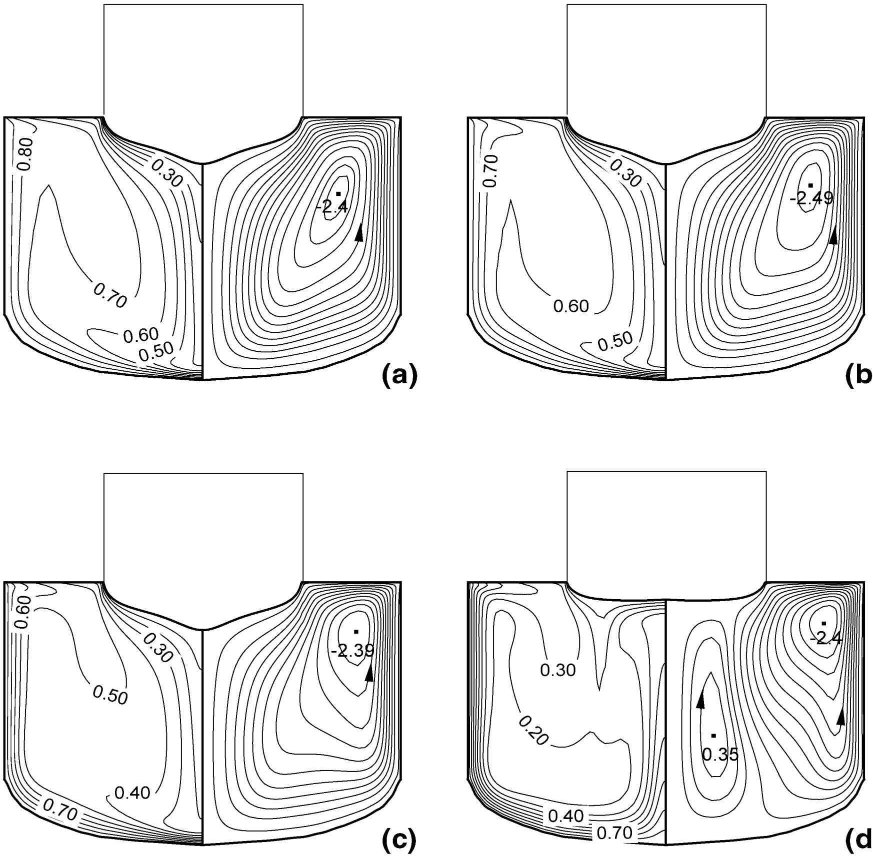

Fig. 6. Effect of absorption on flow and thermal fields in the melt. $Ar = 1.0$, $Rr = 0.5$, $Gr = 2.7 \times 10^4$, $Ma = 535$, $Re_{\mathrm{ct}} = 0$ (no crystal rotation), $\varsigma = 0.0$ (no scattering); (a) $\tau = 0.0$, (b) $\tau = 0.075$, (c) $\tau = 0.25$, (d) $\tau = 0.75$.

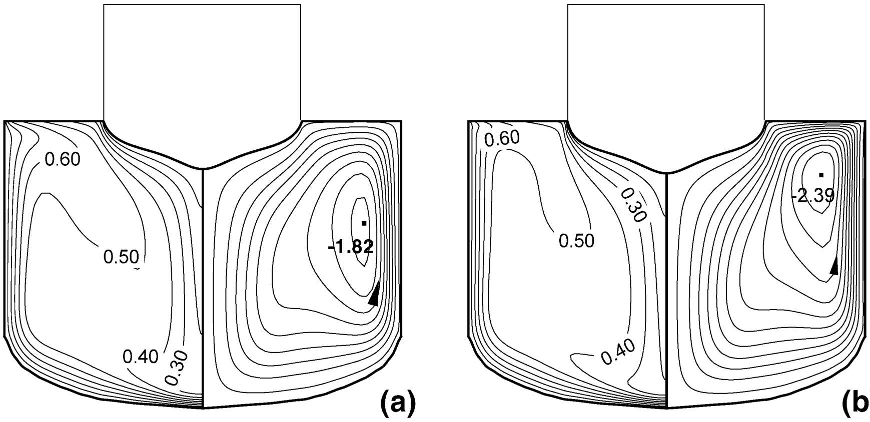

Fig. 7. Effect of Marangoni convection on the flow and thermal fields in the melt. $Ar = 1.0$, $Rr = 0.5$, $Gr = 2.7 \times 10^4$, $Re_{\mathrm{ct}} = 0$ (no crystal rotation), $\varsigma = 0.0$ (no scattering); $\tau = 0.25$, (a) $Ma = 0$, (b) $Ma = 535$.

(Fig. 6(d)) causes the otherwise deeply convex melt–crystal interface to move up along the axis of the crucible.

The effect of increasing Marangoni number on melt convection is brought out in Fig. 7. Surface tension gradients increase shear at the melt–gas interface. Hence the center of the flow pattern shifts vertically upwards. There is a marginal intensification of the flow field as brought out by an increase in the maximum value of the stream function. Thus, buoyancy and surface tension gradients are additive in terms of driving the flow field. The change in the thermal field is, however, marginal, for the range of parameters studied.

Streamlines and isotherms in the YAG melt subject to crystal rotation are shown in Fig. 8. The effect of rotation is to give rise to multiple cells in the crucible, even when the optical thickness is zero. As the optical thickness increases, much of the radiant energy is absorbed near the crucible wall. Hence, the central region between the wall and the axis gets progressively cooler. As a result, the inner

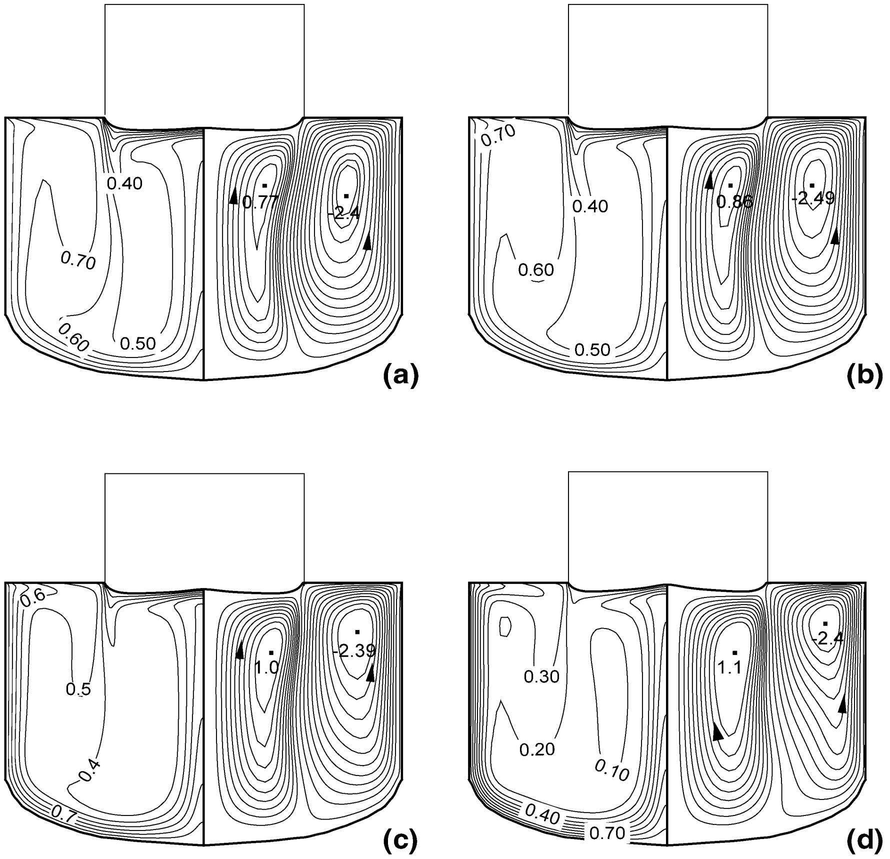

Fig. 8. Effect of absorption on flow and thermal fields in the melt. $Ar = 1.0$, $Rr = 0.5$, $Gr = 2.7 \times 10^4$, $Ma = 535$, $Re_{\mathrm{ct}} = 408$ (with crystal rotation), $\varsigma = 0.0$ (no scattering); (a) $\tau = 0.0$, (b) $\tau = 0.075$, (c) $\tau = 0.25$, (d) $\tau = 0.75$.

forced convection loop gets strengthened. The melt–crystal interface shape is a wavy pattern due to the two convection loops, even when $\tau = 0$. The extent of waviness increases as the optical thickness increases. However, absorption only marginally affects the rotationally driven thermal field. This observation is in agreement with the predictions of Xiao and Derby [2], who reported that the increase in crystal rotation rate does not appreciably change the high thermal gradient melt.

4.2.2. *Effect of scattering*

Scattering of radiation is present in YAG as well as YAG doped with Nd particles. Scattering only redirects the stream of photons; it does not directly affect the energy content of a given volume. Hence, it influences the radiative mode of heat transfer in an indirect manner. While absorbed energy is converted into internal energy of the medium, scattered energy is simply redirected and appears as augmentation along another direction. The re-direction of radiant energy indirectly affects the temperature field in the melt. It is to be noted that the expression for divergence of radiative heat flux (Eq. (4)) does not contain the scattering coefficient. Instead, it comes into picture in RTE (Eq. (5)).

The influence of scattering on the flow and temperature fields in the YAG melt are shown in Fig. 9. The optical thickness of the melt for this sequence of calculations has been kept constant at $\tau = 0.75$ while the scattering coefficient is varied over the range 0–1000 m^{-1}. The corresponding albedo of scattering ($\tilde{\beta}$) varies over 0 to 0.995. The crystal is stationary in these calculations. Broadly speaking, the influence of scattering on the convection patterns is seen to be minor over the range of parameters studied. The influence on the flow and thermal fields is truly insignificant for $\varsigma < 10.0\ \mathrm{m}^{-1}$, namely $\tilde{\beta} < 0.83$. At higher values, scattering is observed to have an opposite influence as compared to absorption. This is understandable because scattering augments the irradiation and penetrates deeper into the crucible, partly nullifying the effect of the absorption coefficient. The augmentation is quite pronounced at high values of the scattering coefficient. The isotherms can be seen to shift towards the colder crystal surface (away from the crucible wall) with an increase in the scattering coefficient. Thus, the thermal gradients tend to spread out more evenly within the crucible. The flow field, initially distorted in the absence of scattering, is more organized, as the scattering coefficient increases. Since the temperature gradients are now present over a greater portion of the crucible cross-section, the intensity of flow field increases (specifically, the magnitude of the stream function) with an increase in the scattering coefficient. The center of the convection cell shifts downwards, towards the axis of the crucible.

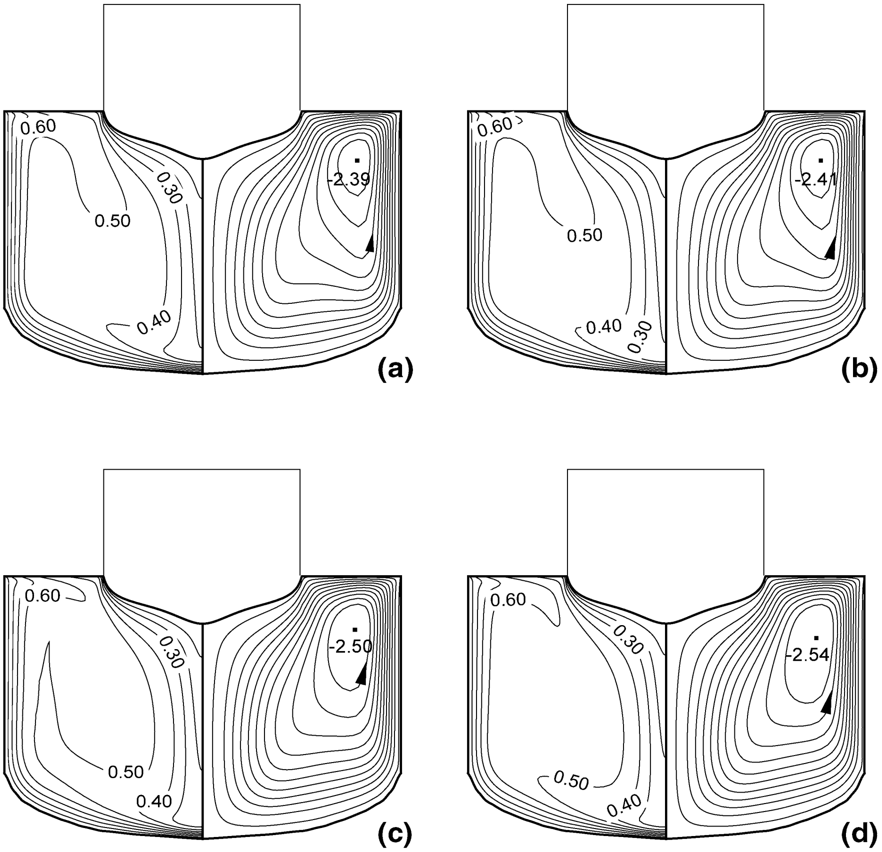

Fig. 9. Effect of scattering on flow and thermal fields in the melt. $Ar = 1.0$, $Rr = 0.5$, $Gr = 2.7 \times 10^4$, $Ma = 535$, $Re_{\mathrm{ct}} = 0$ (no crystal rotation); $\tau = 0.25$, (a) $\varsigma = 0.0\ \mathrm{m}^{-1}$ ($\tilde{\beta} = 0.0$), (b) $\varsigma = 25.0\ \mathrm{m}^{-1}$ ($\tilde{\beta} = 0.83$), (c) $\varsigma = 500.0\ \mathrm{m}^{-1}$ ($\tilde{\beta} = 0.99$), (d) $\varsigma = 1000.0\ \mathrm{m}^{-1}$ ($\tilde{\beta} = 0.995$).

The influence of scattering in a rotationally driven flow field is shown in Fig. 10. The streamlines and isotherms are barely affected till the scattering albedo reaches 0.995. Thus, it can be concluded that the role of scattering is insignificant when the melt is driven by crystal rotation.

4.3. Internal radiation in the presence of crystal and enclosure

In a full Czochralski process, internal radiation is expected to be significant in the grown crystal as well. In the present section, flow and heat transfer in the complete Czochralski system comprising of semi-transparent melt and crystal are considered. The generalized equation of radiative transfer in a discrete direction is solved for the complete domain (involving melt, crystal and gas). Provision is made to account for local radiative properties in the appropriate material, and abrupt changes in radiative properties across the zone boundaries. The intensity field thus obtained is used to evaluate the divergence of the radiative heat flux at all locations in the Czochralski apparatus. The RTE is solved in the entire domain of the apparatus subjected to symmetry boundary condition at the axis, while other walls are assumed to be diffusely emitting and reflecting opaque gray surfaces.

4.3.1. Effect of absorption

Fig. 11 shows streamlines and isotherms when absorption through the crystal alone is considered. The melt is assumed to be transparent ($\kappa_m = 0$) in this calculation. For a higher absorption coefficient of the crystal (κ_c), i.e., for a less transparent crystal, axial heat transfer is augmented by absorption of radiation from the crucible walls. Subsequently, energy is lost to the enclosure, resulting in a lower temperature level in the crystal. The higher average temperature difference between the melt and the crystal marginally increases the strength of melt flow, increasing further with an increase in the absorption coefficient of the crystal. Owing to increased cooling of the crystal the melt–crystal interface moves deeper towards the melt. Since a higher optical thickness cools the crystal, the pull velocity required for the growth of a constant diameter crystal increases with absorption coefficient.

Fig. 12 shows streamlines and isotherms in the growth apparatus, when both the crystal and the melt region are considered to be semi-transparent. The absorption in the melt results in shifting of the isotherms closer to the hot crucible wall. As a result the centre of the convection cell shifts towards the crucible side wall. The strength of flow is diminished as the optical thickness increases, a result discussed in Section 4.2.1. In case of very high absorption, the tempera-

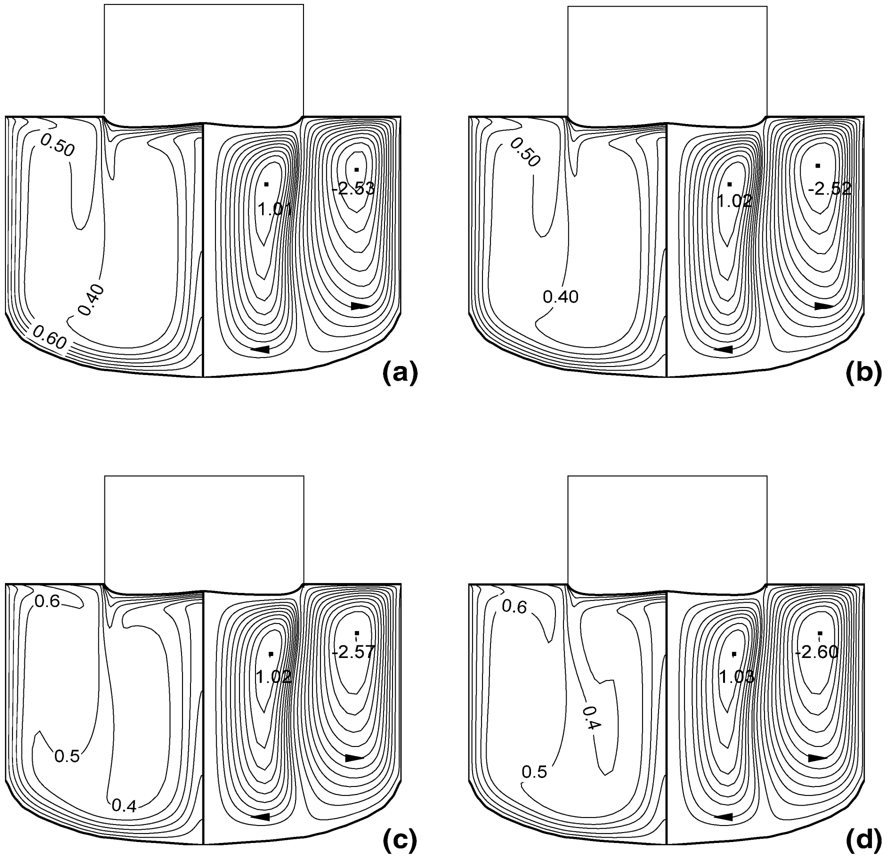

Fig. 10. Effect of scattering on flow and thermal fields in the melt with crystal rotation. $Ar = 1.0$, $Rr = 0.5$, $Gr = 2.7 \times 10^4$, $Ma = 535$, $Re_{\mathrm{ct}} = 408$; $\tau = 0.25$, (a) $\varsigma = 0.0\ \mathrm{m}^{-1}$ ($\tilde{\beta} = 0.0$), (b) $\varsigma = 25.0\ \mathrm{m}^{-1}$ ($\tilde{\beta} = 0.83$), (c) $\varsigma = 500.0\ \mathrm{m}^{-1}$ ($\tilde{\beta} = 0.99$), (d) $\varsigma = 1000.0\ \mathrm{m}^{-1}$ ($\tilde{\beta} = 0.995$).

ture of the central core is low enough, leading to the formation of two convective cells. The solidification of the central core at very high optical thickness cannot be ruled out. When both the melt and crystal have a low optical thickness, the melt–crystal interface is observed to be convex towards the melt. The convexity decreases with an increase in the optical thickness; at very high values, the interface becomes concave. The cooling of the crystal accompanied by the cooling at the core of the crucible results in a significant increase in pull velocity.

The above discussion shows that radiation interactions of significance are between the crucible and the melt on one hand, and the crystal with the enclosure. These influence the shape of the melt–crystal interface and the pull velocity. The direct interaction between the melt and the crystal is only of secondary importance.

4.3.2. Effect of scattering

Scattering has a minor effect on the overall convective field, since it only serves to re-distribute energy. At higher values of optical thickness, the influence of scattering is barely visible. Scattering within the crystal slightly increases its temperature, and results in a marginal reduction in the strength of melt flow. Since the crystal is slightly heated due to scattering, the melt–crystal is less convex. Scattering in the melt, on the other hand, results in heating of the central core below the crystal. The higher temperature difference with respect to the melt–crystal interface leads to an intensification of buoyant flow. A marginal reduction in the pull velocity is seen due to slight heating of the crystal when it acts as a scattering medium. When both the melt and the crystal scatter radiation, there is a marginal increase in the pull velocity. These results have been discussed further in [24].

4.3.3. Influence of crystal length

Fig. 13 shows the temperature distribution and melt flow pattern during two stages of crystal pulling process. These stages correspond to an increase in crystal length and thus a reduction in melt height. At each stage, two separate cases are considered.

(1) Melt is transparent while crystal is semi-transparent ($\tau_c = 0.25$); and
(2) The melt and the crystal are both semi-transparent ($\tau_m = 0.25$, $\tau_c = 0.25$).

It can be observed that at both stages, the strength of flow marginally increases when the crystal is semi-transparent, while the combined effect of absorption in both the melt and crystal is to cool the core of the melt in the crucible. This retards the strength of flow. At the last stage of growth

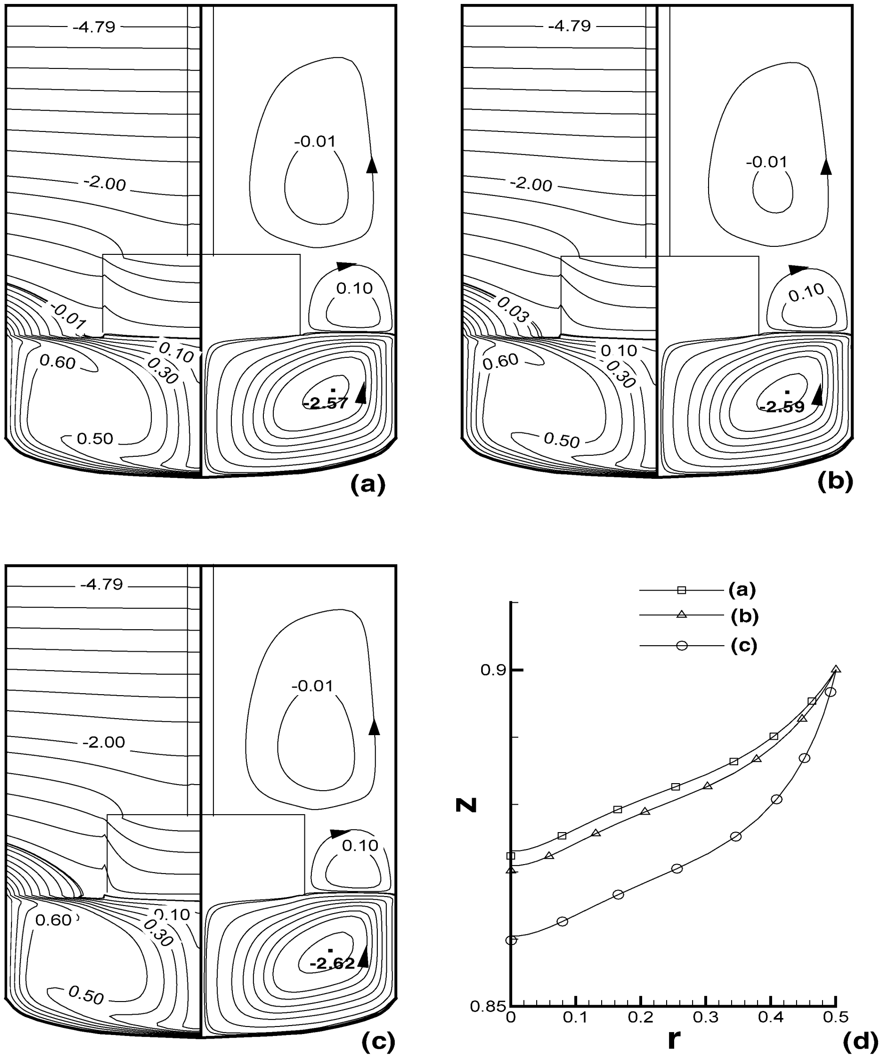

Fig. 11. Effect of absorption in the crystal on flow and thermal fields in the full domain of the Czochralski apparatus. $Ar = 0.9$, $Rr = 0.5$, $Hr = 0.5$, $T_\infty = 1400$ K, $T_w = 2403$ K, $Gr = 2.16 \times 10^4$, $Ma = 475$, $Re_{\mathrm{ct}} = 0$ (stationary crystal), $\tau_m = 0.0$; (a) $\tau_c = 0.075$, (b) $\tau_c = 0.75$, (c) $\tau_c = 5.0$, (d) melt–crystal interface shapes for (a)–(c).

(very low melt height), the cooling of the core results in the development of two convective cells in the crucible. The melt–crystal interface gets deeply convex towards the melt due to absorption in the crystal. When both the melt and the crystal are semi-transparent, the cooling at the core results in inversion of the melt–crystal interface. This shows that enclosure temperature can certainly be used to control losses from the melt and the crystal, even when the media are radiatively participating. The enclosure temperature provides an extra degree of freedom to adjust the interface shape.

4.3.4. *Effect of absorption and scattering on pull velocity*

One of the significant aspects of the Czochralski process is the need to control pull velocity so as to grow a constant diameter crystal. If the pull velocity is high in comparison to the crystallization speed, the diameter progressively diminishes. Conversely, there is an increase in the crystal diameter. The correct pull velocity can be obtained by applying the Stefan condition for change of phase from the melt to the crystal [27]. This condition requires that the difference between the melt and the crystal heat fluxes is balanced by the rate of latent heat release. Clearly, changes in the heat fluxes in the respective phases, possibly due to absorption and scattering, affect the pull velocity. Specifically, a higher temperature gradient in the crystal raises the pull velocity. In the present study, the pull velocity required to maintain a constant crystal diameter has been evaluated at the edge of the crystal.

Pull velocity has been observed to increase with an increase in the optical thickness either in the melt or the crystal. As the absorption in the crystal is increased the heat flux through the crystal also increases, resulting, in an increase in the pull velocity. An increase in absorption in the melt on the other hand displaces the isotherms towards the crucible wall, thereby decreasing the heat flux from the melt side. This in

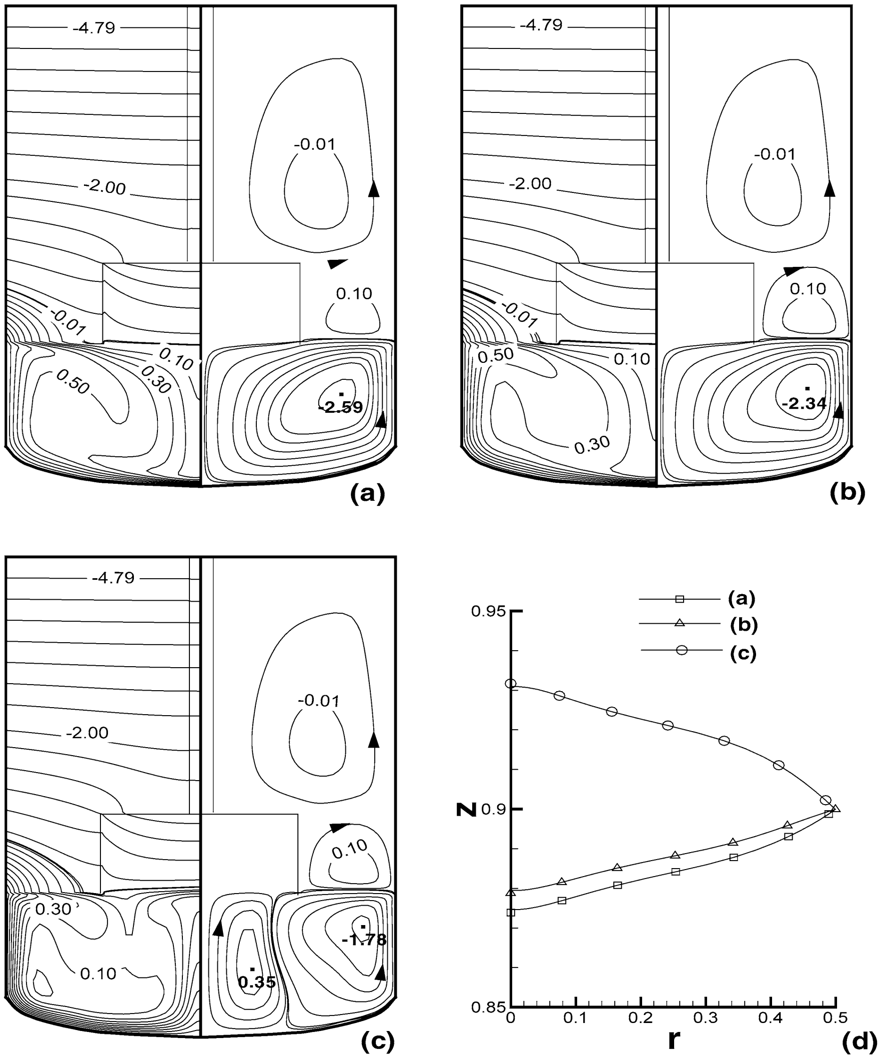

Fig. 12. Effect of absorption in both the melt and the crystal phase, on flow and thermal fields in the full domain of the Czochralski apparatus. $Ar = 0.9$, $Rr = 0.5$, $Hr = 0.5$, $T_\infty = 1400$ K, $T_w = 2403$ K, $Gr = 2.16 \times 10^4$, $Ma = 475$, $Re_{\mathrm{ct}} = 0$ (stationary crystal); (a) $\tau_c = 0.075$, $\tau_m = 0.075$, (b) $\tau_c = 0.25$, $\tau_m = 0.25$, (c) $\tau_c = 0.75$, $\tau_m = 0.75$, (d) melt–crystal interface shapes for (a)–(c).

turn increases the pull velocity. Thus, the combined effect of absorption in the melt as well as the crystal is to raise the pull velocity required for maintaining a constant crystal diameter. For an increase in the optical thickness from zero to 0.75 in the melt and the crystal, the pull velocity was found to increase from 1.2 mm·h^{-1} to 2.8 mm·h^{-1}, for the parameters in Fig. 11.

Scattering has an opposite effect on pull velocity variation. Scattering in the crystal heats up the crystal leading to a reduction in the interfacial heat flux and hence the pull velocity.

4.3.5. Effect of crystal rotation

As the crystal is rotated, fluid particles in the melt acquire a tangential velocity component in the horizontal plane, that in turns sets up a radially outward component of acceleration. This creates a low pressure region below the crystal. Consequently, the hot melt from the base of the crucible moves vertically upwards, along the crystal axis. The convective cell thus formed is in the clockwise direction. The resulting isotherms are pushed up along the centre-line of the crucible and the high temperature melt is moved radially along the crystal boundary. Under these conditions, thermal gradients are predominantly fixed by the mixing of fluid particles induced by rotation. Consequently, the effect of absorption (as well as scattering) is minimal in a rotationally driven flow field.

5. Conclusions

The effects of internal radiation in the Czochralski process on flow and thermal fields in the melt as well as the overall growth process have been studied. The convective field is sensitive to the optical thickness, but depends only weakly on the scattering albedo. Absorption in the

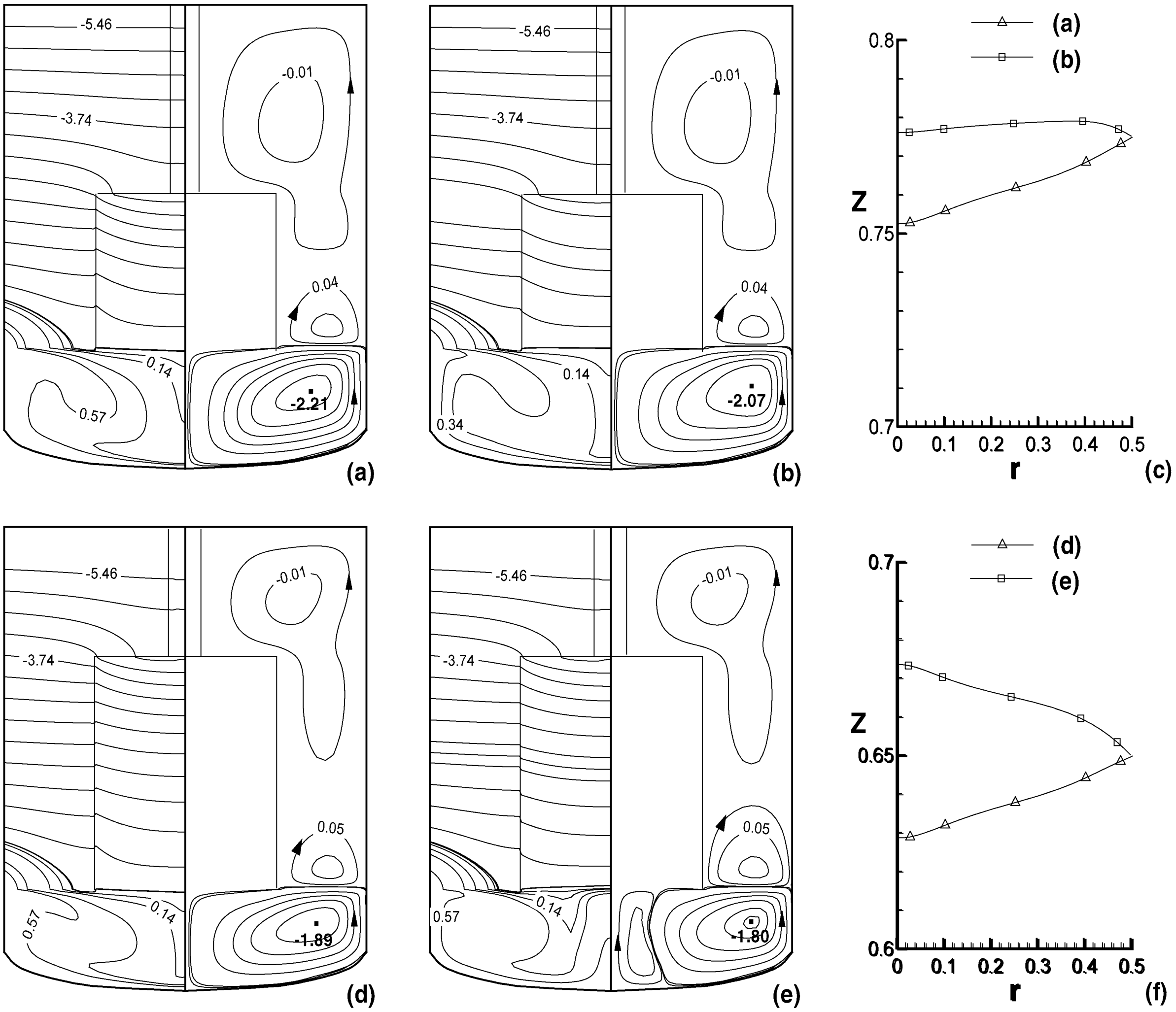

Fig. 13. Effect of absorption in the melt and crystal on flow and thermal fields in the full domain of the Czochralski process with increase in crystal length; $Rr = 0.5$, $T_\infty = 1400$ K, $T_w = 2403$ K, $Gr = 2.16 \times 10^4$, $Ma = 475$, $Re_{\mathrm{ct}} = 0$, (a) $Ar = 0.775$, $Hr = 1$, $\tau_c = 0.25$, $\tau_m = 0$, (b) $Ar = 0.775$, $Hr = 1$, $\tau_c = 0.25$, $\tau_m = 0.25$, (c) melt–crystal interface shapes for (a), (b). (d) $Ar = 0.65$, $Hr = 1.5$, $\tau_c = 0.25$, $\tau_m = 0$, (e) $Ar = 0.65$, $Hr = 1.5$, $\tau_c = 0.25$, $\tau_m = 0.25$, (f) melt–crystal interface shapes for (d), (e).

melt is a maximum near the hot crucible walls. As the optical thickness increases, densely packed isotherms near the crucible wall are formed. For very high absorption, a low temperature region is formed at the core of the crucible. Intense cooling of the core at a high value of optical thickness generates two convective cells in the melt flow. As a consequence a wavy shape of the interface, concave at the center and convex towards the edge of the crystal is observed.

Influence of scattering on the convective field in the melt is observed only at high values of the scattering albedo. With an increase in scattering, the isotherms are seen to shift towards the colder crystal surface (away from the crucible wall). As a consequence there is a slight increase in the strength of the flow field and a shift in the center of the convection loop. In addition, the convexity of the melt–crystal interface is slightly reduced.

Absorption results in cooling of the crystal and increases the pull velocity required for growth of a constant diameter crystal. The melt–crystal interface gets deeply convex due to crystal cooling. Scattering on the other hand results in marginal heating of the crystal. The combined effect of absorption in the melt and crystal can lead to solidification of the melt at its core. The temperature of the enclosure is seen to influence the melt–crystal interface shape when absorption in both the crystal and the melt are considered.

The impact of internal radiation diminishes in the presence of crystal rotation.

Acknowledgement

The authors thank the referees for their detailed comments and suggestions.

References

[1] Q. Xiao, J.J. Derby, The role of internal radiation and melt convection in Czochralski oxide growth: Deep interfaces, interface inversion and spiraling, J. Crystal Growth 128 (1993) 175–188.

[2] Q. Xiao, J.J. Derby, Heat transfer and interface inversion during the Czochralski growth of Yttrium aluminum garnet and Gadolinium Gallium garnet, J. Crystal Growth 128 (1993) 188–213.

[3] J.J. Derby, Q. Xiao, Some effects of crystal rotation on large-scale Czochralski oxide growth: Analysis via hydrodynamic thermocapillary model, J. Crystal Growth 113 (1991) 575–586.

[4] T. Tsukada, K. Kakinoki, M. Hozawa, Effect of internal radiation within crystal and melt on Czochralski crystal growth of oxide, Internat. J. Heat Mass Transfer 38 (1995) 2707–2714.

[5] M. Kobayashi, T. Tsukada, M. Hozawa, Effect of internal radiative heat transfer on the convection in Czochralski oxide melt, J. Crystal Growth 180 (1997) 157–166.

[6] E.M. Nunes, H.N. Mohammad, H.N. Naraghi, H. Zhang, V. Prasad, A volume radiation heat transfer model dor Czochralski crystal growth process, J. Crystal Growth 236 (2002) 596–608.

[7] V. Prasad, H. Zhang, A.P. Anselmo, Transport phenomena in Czochralski crystal growth processes, Adv. Heat Transfer 30 (1997) 314–435.

[8] M. Kobayashi, T. Hagino, T. Tsukada, M. Hozawa, Effect of internal radiative heat transfer on interface inversion in Czochralski crystal growth of oxides, J. Crystal Growth 235 (2002) 258–270.

[9] R. Krishnamurti, On the transition to turbulent convection. Part 1. Transition from two to three-dimensional flow, J. Fluid Mech. 42 (1970) 295–307.

[10] B. Gebhart, Y. Jaluria, R.L. Mahajan, B. Sammananka, Buoyancy-Induced Flows and Transport, Hemisphere, Washington, DC, 1988.

[11] N.C. Markatos, K.A. Pericleous, Laminar and turbulent natural convection in an enclosed cavity, Internat. J. Heat Mass Transfer 27 (1984) 755–772.

[12] M.F. Modest, Radiative Heat Transfer, McGraw-Hill Book Company, New York, 1993.

[13] M.N. Ozisik, Radiative Transfer and Interactions with Conduction and Convection, Wiley, New York, 1973.

[14] R. Siegel, J.R. Howell, Thermal Radiation Heat Transfer, McGraw-Hill Book Company, New York, 1984.

[15] S. Chandrasekhar, Radiative Transfer, Dover, London, 1960.

[16] K.D. Lathrop, B.G. Carlson, Discrete-ordinates angular quadrature of the neutron transport equation, Technical information series report LASL-3186, Los Alamos Scientific Laboratory, 1965.

[17] J. Pessoa-Filho, S.T. Thynell, Approximate solution to the equation of radiative transfer in cylindrical participating media, J. Quantit. Spectrosc. Radiat. Transfer 53 (1995) 533–547.

[18] J. Menart, J. Heberlein, E. Pfender, Theoretical radiative transport results for a free burning arc using a line-by-line technique, J. Physics 32 (1999) 55–63.

[19] J. Menart, Radiative transport in a two-dimensional axisymmetric thermal plasma using the S–N discrete ordinates method on a line-by-line basis, J. Quantit. Spectrosc. Radiat. Transfer 67 (2000) 273–291.

[20] S.S. Dua, P. Cheng, Multi-dimensional radiative transfer in non-isothermal cylindrical media with non-isothermal bounding walls, Internat. J. Heat Mass Transfer 18 (1975) 245–259.

[21] P. Hintz, D. Schwabe, H. Wilke, Convection in a Czochralski crucible, Part I: Non-rotating crystal, J. Crystal Growth 222 (2001) 343–355.

[22] H.J. Sung, Y.J. Jung, H. Ozoe, Prediction of transient oscillating flow in Czochralski convection, Internat. J. Heat Mass Transfer 38 (1995) 1627–1636.

[23] A.A. Mohamad, Benchmark solution for unsteady state CFD problems, Numer. Heat Transfer A 34 (1998) 653–672.

[24] J. Banerjee, Czochralski growth of oxide crystals: Numerical simulation and experiments, PhD thesis, Indian Institute of Technology, Kanpur, 2005.

[25] J. Lu, M. Prabhu, J. Song, C. Li, J. Xu, Optical properties and highly efficient laser oscillation of Nd:YAG ceramics, J. Appl. Phys. B 71 (2000) 469–473.

[26] J. Kvapil, J. Kvapil, B. Manek, B. Perner, R. Autrata, P. Schauer, Czochralski growth of YAG:Ce in a reducing protective atmosphere, J. Crystal Growth 52 (1981) 542–545.

[27] H. Kopetsch, Numerical simulation of interface inversion in Czochralski growth of oxide crystals, J. Crystal Growth 102 (1990) 505–528.